

Reconciling different observational data sets from Surface Heat Budget of the Arctic Ocean (SHEBA) for model validation purposes

H. Huwald¹

Institute for Atmospheric and Climate Science, Swiss Federal Institute of Technology, Zurich, Switzerland

L.-B. Tremblay

Lamont-Doherty Earth Observatory, Columbia University, Palisades, New York, USA

H. Blatter

Institute for Atmospheric and Climate Science, Swiss Federal Institute of Technology, Zurich, Switzerland

Received 21 November 2003; revised 24 November 2004; accepted 19 January 2005; published 14 May 2005.

[1] Observations from the Surface Heat Budget of the Arctic Ocean (SHEBA) are analyzed to develop a consistent data set suitable for the validation of snow and sea ice components used in climate models. Since the snow depth is a crucial variable to properly determine the ice thickness evolution, several methods are tested to estimate the actual snow depth at the exact location of the measured internal temperatures. Snow and ice thickness gauge measurements show high spatial variability at small spatial scales. Consequently, individual measurements of snow/ice thickness are not representative of the thickness at the locations where temperature profiles were measured. Observed skin temperatures and snow internal temperature profiles suggest that the mean winter snow cover at the reference mass balance site was thicker by 11 cm when compared with gauge observations at a small distance from that reference site. The mean winter snow cover thickness measured at the SHEBA mass balance site, Pittsburgh, is larger by a factor of 2.3 when compared to the snow depth derived from precipitation measurements. Assuming continuity of heat fluxes at the snow-ice interface, an effective snow thermal conductivity of $0.50 \text{ Wm}^{-1} \text{ K}^{-1}$ is calculated. This is significantly higher than values generally used in climate models ($0.31 \text{ Wm}^{-1} \text{ K}^{-1}$) or derived from in situ measurements ($0.14 \text{ Wm}^{-1} \text{ K}^{-1}$) at SHEBA. Ocean heat fluxes, inferred from ice thickness and internal temperature measurements at various sites, are very consistent and match reasonably well those derived from turbulence measurements and a bulk formulation. A heat budget of surface fluxes shows a mean annual net imbalance of 1.5 Wm^{-2} , with a mean energy deficit of 3.5 Wm^{-2} during winter and a mean surplus of 6.4 Wm^{-2} during summer.

Citation: Huwald, H., L.-B. Tremblay, and H. Blatter (2005), Reconciling different observational data sets from Surface Heat Budget of the Arctic Ocean (SHEBA) for model validation purposes, *J. Geophys. Res.*, *110*, C05009, doi:10.1029/2003JC002221.

1. Introduction

[2] Global climate models predict a polar amplification of the warming signal associated with anthropogenic forcing. The magnitude of this warming however, is uncertain and depends mainly on the response of the snow, sea-ice and cloud components in these models. To provide better

estimates of future climate and climate changes, measurements of surface energy fluxes and mass balance at high latitudes are crucial. Measurements can be used to validate the snow and sea ice components used in climate models and test their ability to simulate observed conditions and changes in these regions.

[3] Observations from the Surface Heat Budget of the Arctic Ocean (SHEBA) field experiment [Perovich *et al.*, 1999a; Uttal *et al.*, 2002] constitute such a data set. The measurements were made in the Beaufort and Chukchi seas and spanned almost an entire year (end of October 1997 to mid-October 1998). These observations make it possible to test sea ice models off-line over a full annual cycle. Although SHEBA provides the most comprehensive data

¹Now at Environmental Fluid Mechanics Laboratory, Ecole Polytechnique Federale de Lausanne, Lausanne, Switzerland.

set for model development and testing, several factors still need to be considered before this data set can be used for the validation of thermodynamics sea ice models.

[4] For instance, high variability in the snow and ice cover thickness is present at relatively small spatial scales (of the order of meters [see, e.g., *Sturm et al.*, 2002a; *Comiso et al.*, 1991]). Since the ice thickness evolution depends (among other things) on the thickness of the snow cover, and since internal temperature profiles provide a very useful constraint to test the ability of a model to simulate the ice growth evolution, it is important to measure snow depth, ice thickness and internal ice temperature at the same location. Moreover, a characterization of this spatial variability will be important to quantify potential departure from the purely one-dimensional heat conduction problem implied by column measurements such as those made at SHEBA.

[5] There are also significant uncertainties in snow fall measurements. Uncorrected measurements of snow precipitation usually underestimate the accumulation at the surface in the Arctic [*Walsh et al.*, 1998]. In fact, low correlation between cumulative precipitation and snow depth measurements was noted by *Colony et al.* [1998]. Undercatch due to wind effects [*Yang*, 1999], and blowing snow effects [*Sturm et al.*, 2002a; *Déry and Tremblay*, 2004] can account for some of the discrepancies between measured precipitation and observed snow depth. Apart from the systematic errors that may be involved, a point measurement is not always representative of the actual snow cover thickness in a given area due to the high variability at small spatial scales. In this study, the snow thickness measurements at SHEBA will be carefully examined and adjusted, based on a detailed analysis of observed internal snow and sea ice temperatures.

[6] There is also uncertainty in the interpretation of the snow thermal conductivity, and consequently the magnitude of heat conduction through snow. In a snow cover, heat is transported by conduction, but also by advection and latent heat release associated with wind pumping and transport of moist air within the snow. Atmospheric conditions such as low-level wind, air temperature and humidity will effect the advective and diffusive transport of moist air within the snowpack resulting in an “apparent” (effective) thermal conductivity larger than the pure value. The snow thermal conductivity has been determined in numerous studies using data from both field and laboratory experiments [*Sturm et al.*, 1997]. Most of these parameterizations describe the snow thermal conductivity as a function of snow density and temperature, although other physical properties such as the bonding of individual grains influence the pure thermal conductivity. A review by *Sturm et al.* [1997] shows that differences in snow microphysical properties can result in an order of magnitude range in conductivity at a given density.

[7] In situ measurements of snow thermal conductivity at SHEBA are very consistent with a mean and a standard deviation of $0.14 \text{ Wm}^{-1} \text{ K}^{-1}$ and $0.03 \text{ Wm}^{-1} \text{ K}^{-1}$ respectively [*Sturm et al.*, 2001]. The bulk thermal conductivity (inferred from snow depth, basal ice growth, ocean heat flux, and air and snow-ice interface temperatures) at 15 locations of the mass balance sites Baltimore, Seattle and the Ridge however [*Sturm et al.*, 2002b], ranges from $0.17 \text{ Wm}^{-1} \text{ K}^{-1}$ to $0.70 \text{ Wm}^{-1} \text{ K}^{-1}$. During their 1993/94 measuring cam-

paign, *Perovich et al.* [1997] inferred snow thermal conductivities of about $0.3 \text{ Wm}^{-1} \text{ K}^{-1}$ from internal temperature profiles in the Beaufort Sea, assuming a continuity of heat fluxes at the snow-ice interface.

[8] Applying a detailed one-dimensional model for polar snow covers (SNThERMP), *Jordan et al.* [2003] investigated the temporal evolution of the snow thickness and the heat transfer through the snow cover at the SHEBA site Pittsburgh. They found that during winter a thermal conductivity of at least $0.33 \text{ Wm}^{-1} \text{ K}^{-1}$ is required to extract enough heat from the snow cover, and simulate the observed snow-ice interface temperatures accurately. Current modeling practice typically uses a midrange value of snow thermal conductivity around $0.30 \text{ Wm}^{-1} \text{ K}^{-1}$ [*Bitz and Lipscomb*, 1999; G. A. Schmidt, personal communication, 2003]. In the present study, the snow thermal conductivity is evaluated indirectly from observed snow/ice internal temperature profiles (assuming continuity of conductive heat fluxes [*Perovich et al.*, 1997]) at several SHEBA sites, and its effect on the surface heat balance is evaluated.

[9] The focus of the present paper is on the development of a consistent forcing and validation data set from the SHEBA mass balance site Pittsburgh, to be used for model validation purposes (e.g., the Sea Ice Model Intercomparison Project, Part 2, Thermodynamics (SIMIP2)). A self-consistency check of independent but related observations allows to identify less representative data sets, and to propose corrections for those same variables. To this end, a careful analysis of snow depth, precipitation and snow/ice internal temperatures is presented. A complete surface and basal heat budget is also presented as a measure of the internal consistency of the new proposed data set. In a companion paper, *Huwald et al.* [2005] present the validation of a sigma-coordinate thermodynamic sea ice model forced with the data presented herein. Results presented by *Huwald et al.* [2005] provide indirect evidence for the internal consistency of the proposed data set.

[10] The outline of the paper is as follows. In section 2, all relevant observations used in the data analysis and the energy budget are documented. Section 3 discusses the self-consistency of the forcing and validation data sets. This section includes the determination of the ice (section 3.1) and snow (section 3.2) thickness at the thermistor string location, and the investigation of the snow thermal conductivity from internal temperature profiles (section 3.3). The surface and basal heat budgets and problems associated with the closing of the budgets, are presented in sections 4 and 5. Finally, section 6 summarizes the most important findings and conclusions.

2. Surface Heat Budget of the Arctic Ocean (SHEBA) Data Description

[11] The SHEBA field experiment covered almost an entire annual cycle from late October 1997 to mid-October 1998 in the Beaufort and Chukchi seas of the Arctic Ocean. Part of the data used in this study is taken from an integrated data set (from SHEBA) which was compiled for SIMIP2 (<http://acsys.seos.uvic.ca/acsys/simip2>). More comprehensive SHEBA data sets are available through the Joint Office of Science Support/University Corporation for Atmospheric Research (JOSS/UCAR). Apart from the SIMIP2 data set,

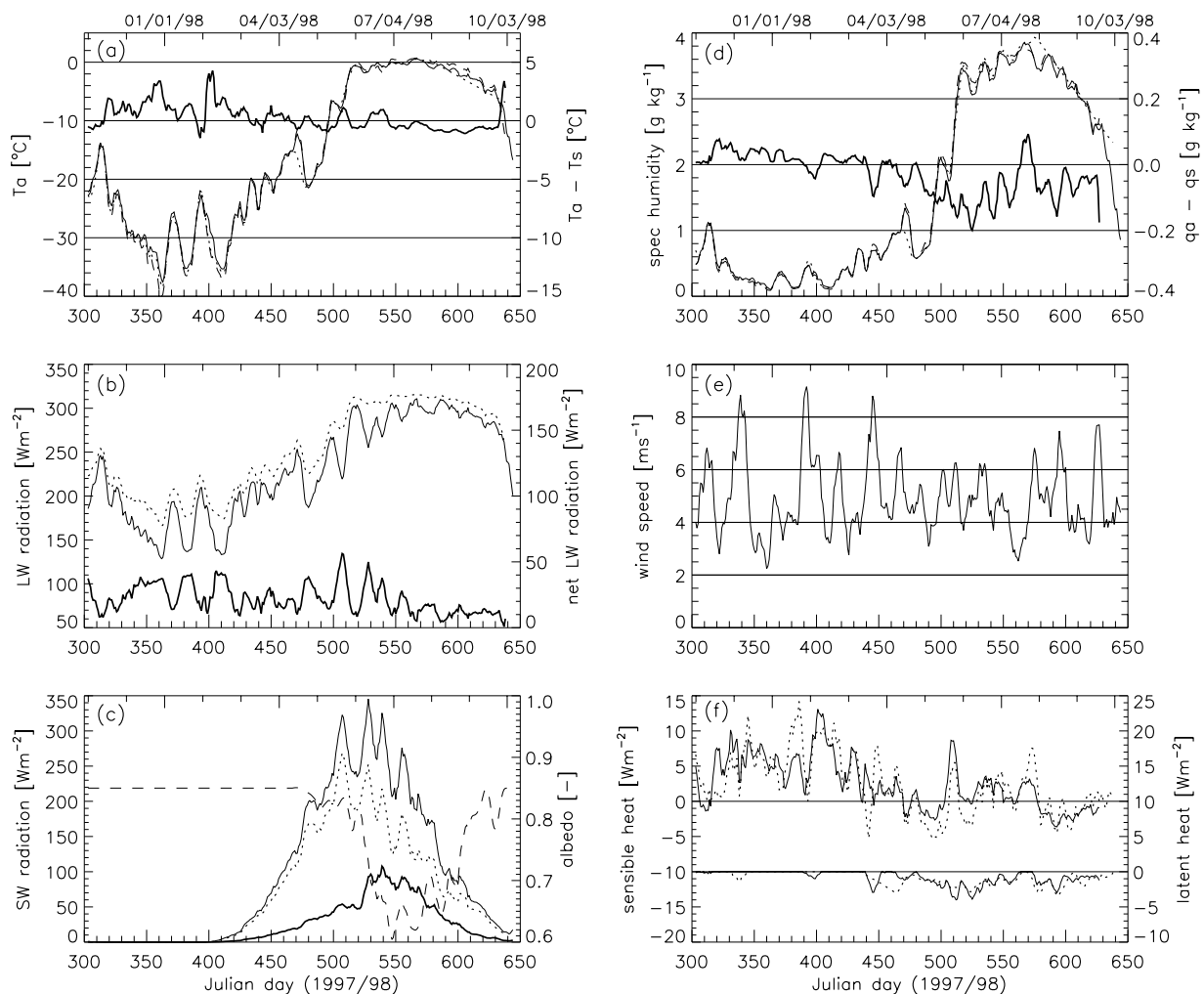


Figure 1. Annual cycle of (a) 10 m air temperature (T_a , solid line), skin temperature (T_s , dotted line), and the temperature difference $T_a - T_s$ (bold solid line), (b) downward (solid line), upward (dotted line), and net (bold solid line) longwave radiation, (c) downward (solid line), upward (dotted line), and net (bold solid line) shortwave radiation, and albedo (dashed line), (d) 10 m specific air humidity (q_a , solid line), surface specific humidity (q_s , dotted line), and the specific humidity difference $q_a - q_s$ (bold solid line), (e) 10 m wind speed, and (f) sensible and latent heat flux calculated using eddy correlation (dotted line) and bulk parameterization using 10 m atmospheric data (solid line) provided by the Sea Ice Model Intercomparison Project, Part 2, Thermodynamics (SIMIP2). In Figure 1f the two curves at the top are for the sensible heat, and the two curves at the bottom are for the latent heat. Turbulent heat fluxes are defined positive toward the surface. All variables are smoothed using a 7 day running mean. Julian day zero is defined as 1 January 1997, 0000 LT.

all data used in this study are available at the JOSS/UCAR web site (<http://www.joss.ucar.edu/cgi-bin/codiac/projs?SHEBA>).

[12] The atmospheric part of the SIMIP2 data set was measured at the 20 m meteorological tower of the Atmospheric Surface Flux Group (ASFG) [Persson *et al.*, 2002]. Data include 10 m wind speed, air temperature and humidity, and the precipitation rate. Radiative fluxes include shortwave and longwave radiation which were measured 2 m above ground, at a distance of about 25 m from the base of the ASFG tower. The albedo provided in SIMIP2 was measured by the Ice Physics Group (IPG) at a point close to the SHEBA mass balance site Pittsburgh on an undeformed multiyear ice floe covered by snow during winter, and

without melt ponds in the summer [Perovich *et al.*, 1999b, 2002a]. Albedo measurements were made from 16 April 1998 through 28 September 1998, with a sampling frequency of two days from 25 May to 9 September, and lower frequency (2–8 days) during the rest of the observation period. Before 16 April and after 28 September, SIMIP2 proposes a constant albedo of 0.85 in agreement with measured albedo values from late spring and early fall.

[13] Following Perovich and Elder [2002], ocean heat fluxes for SIMIP2 were calculated as the residual between the conductive heat fluxes and the latent heat released or absorbed (associated with growth and melt) at the ice base. Internal snow/ice temperature measurements from several SHEBA sites are used to derive surface and basal conduc-

tive fluxes. Snow and ice thickness observations made throughout the year are used to calculate the energy of melt (or growth) in the energy budget. Finally, turbulence measurements in the upper ocean derived from eddy correlation technique [McPhee, 2002] and a bulk formulation [McPhee et al., 2003] have been used for comparison with those calculated here and those provided by SIMIP2.

[14] In addition to the SIMIP2 data set, skin (surface) temperatures, from Portable Automated Mesonet (PAM) stations at the SHEBA sites “Atlanta,” “Baltimore,” “Florida,” and the ASFG tower site [Persson et al., 2002], are used for the calculation of the turbulent heat fluxes, and as an additional constraint to locate the snow surface elevation from measured internal snow/ice temperature. The sensible and latent heat fluxes are calculated using standard bulk formulations from the 10 m air temperature, humidity, wind speed measured at the ASFG tower, and the surface temperatures from the PAM stations. Atmospheric turbulent heat fluxes derived from high-frequency measurements of the same quantities made at the ASFG tower [Persson et al., 2002] are also used for comparison. All SIMIP2 data are provided with a time resolution of one hour, nearly covering a complete annual cycle (31 October 1997–8 October 1998). Lower-temporal-resolution data such as the surface albedo and the ocean heat flux are linearly interpolated down to one hour.

[15] The observed time series are shown in Figure 1. The downward longwave radiation mainly follows the pattern of the air temperature (Figures 1a–1b). High (low) values of the incident shortwave radiation correspond with low (high) values of the downward longwave radiation due to the absence (presence) of clouds. During cloudy periods, the net longwave radiation is very small. The albedo is at 0.85 during the cold season, decreases slightly to 0.81 when the daily temperature approaches the freezing point and the snow surface gets warmer, and drops rapidly when the surface gets wet at the beginning of June.

[16] During winter, the specific humidity is generally below 1 g kg^{-1} and increases in spring together with the air temperature. The surface relative humidity, defined with respect to ice saturation (not shown here), remains near 100% throughout the year as discussed by Andreas et al. [2002]. The sensible heat flux depends on both the wind speed and the difference between the air and skin temperature which in turn depends on the presence of clouds [Walsh and Chapman, 1998]. The latent heat flux mainly shows a dependence on the difference between 10 m and surface specific humidities, with a peak in June indicating an increase in surface evaporation/sublimation during that period. Both turbulent heat fluxes generally show a similar pattern, although they differ in magnitude.

[17] The internal snow and ice temperatures were measured at 7 mass balance sites [Perovich et al., 1999b], 6 of which were used in the present study (Figure 2). One site was located on a 7 m ridge and is not considered here. The 6 sites were located around the SHEBA camp and represent a variety of ice types: “Baltimore” (first-year ice), “Pittsburgh” (snow covered multiyear ice), “Quebec 1” and “Quebec 2” (young ice and multiyear ice with little snow), “Seattle” (ponded ice), and “Tuk” (consolidated ridge).

[18] Measurements were performed over an annual cycle using thermistor strings (thermistors mounted in a plastic

pipe) that extend about a meter below the ice base down into the ocean mixed layer, and up to a few decimeters (depending on snow depth) into the air above the snow or ice surface [Perovich and Elder, 2001]. The vertical resolution (given by the thermistor spacing) is 10 cm, and the length of a given thermistor string is 1 m. To cover the full extent of the snow and ice layer, several strings were attached one at the end of the other. At some sites (Pittsburgh and Quebec 2), two overlapping strings with an offset of 5 cm were used to increase the resolution just above and below the snow-ice interface. In both cases, there were consistent biases in the instruments resulting in sawtooth shaped temperature profiles with amplitudes of up to several tenths of a degree.

[19] The accuracy of the thermistors was 0.1°C . However in practice their accuracy is probably worse for several reasons. The devices have no radiation shielding, and the polyvinyl-chloride rod itself and the wires connecting the thermistors conduct heat. Radiation effects are only important in the summer and can lead to errors of a few degrees. To minimize the conduction effects, the plastic rod thermal conductivity was chosen to be similar to that of ice. Heat conduction in the wires can result in substantial errors in thin ice (0–40 cm) with the thermistors reading up to a couple of degrees colder, whereas in thicker ice (as at SHEBA) the thermistor temperatures are quite accurate (D. K. Perovich, personal communication, 2004). Measurements made by the thermistors in the air and in the near-surface snow during summer daylight hours are probably high because of radiation effects and conduction through the pipe.

[20] Locations where the snow and ice thicknesses were measured during the SHEBA experiment are called mass balance sites. There were more than 100 mass balance sites deployed on a variety of ice types at SHEBA, ranging from thin first-year ice to thick multiyear ice. For snow and ice thickness measurements, three gauges were typically set up around the thermistor string (at least 1 m away) forming a triangular cluster [Perovich and Elder, 2001]. In some cases, there were many thickness gauges in the vicinity of a thermistor string. In this study, the three closest gauges to the thermistor string were used, except for Seattle and Tuk where six and five gauges, respectively, have been taken into account.

[21] Snow depth was measured with snow stakes frozen into the ice. Ice thickness was measured using hot wire gauges adjacent to the stakes. Accuracies of the stakes and wire measurements are about 1 cm. The snow cover disappeared completely during the melt season. Considering all measurement sites at SHEBA, the average winter snow cover thickness was 34 cm with a mean bulk density of 320 kg m^{-3} [Sturm et al., 2001]. Thus the complete melting of this snow layer corresponds to an average surface ablation of 11 cm snow water equivalent.

[22] The internal snow/ice temperatures were measured automatically every hour, whereas the thickness data were usually collected once every 1–2 weeks during winter, and once every two days during the summer. The temperature measurements at the various mass balance sites started in late October 1997 and ran until mid-September 1998 which gives a record length of almost 11 months. The individual sites at SHEBA were exposed to relatively uniform forcing.

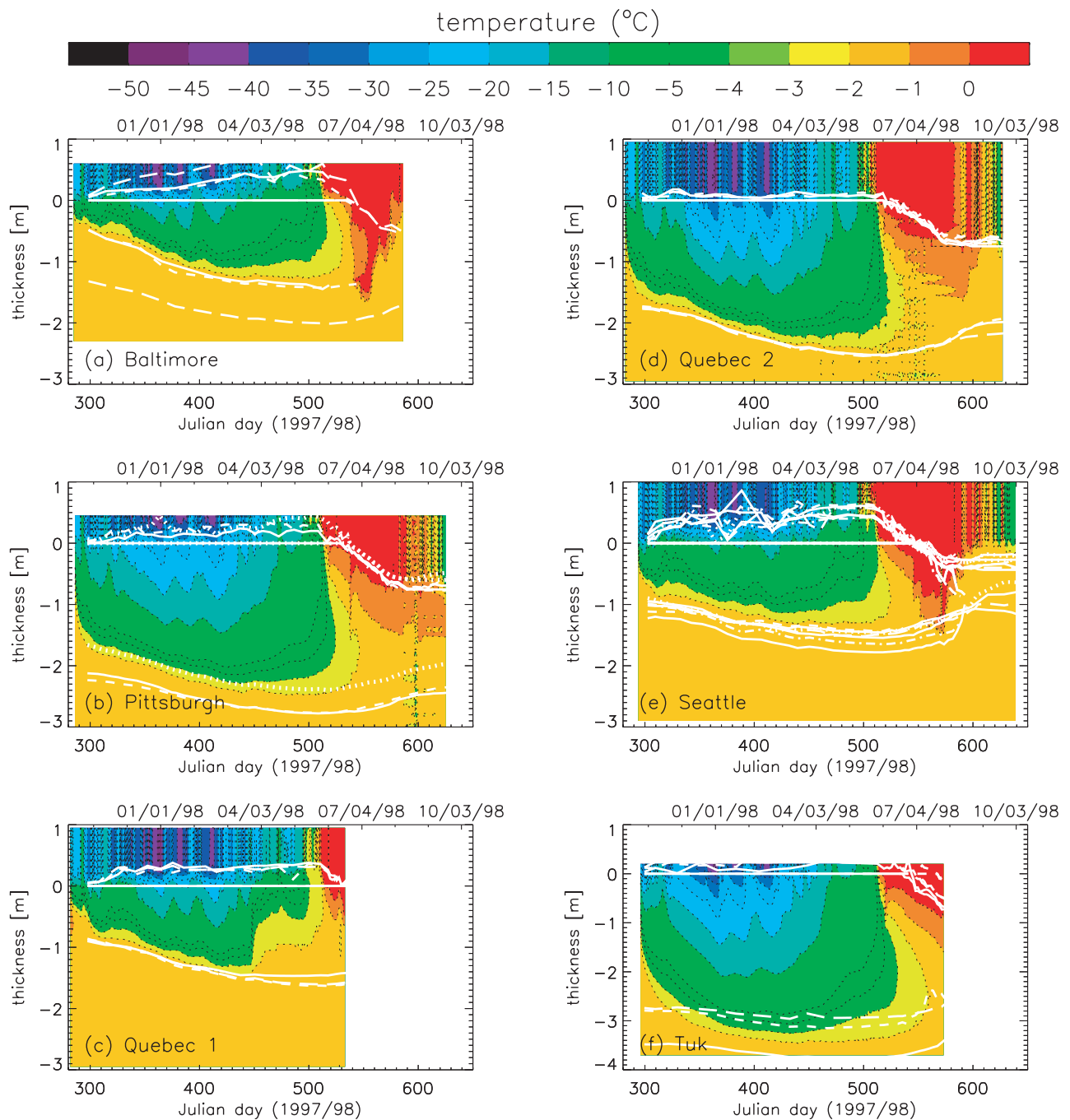


Figure 2. Thermistor string internal temperatures and measured snow surface, ice surface, and ice base evolutions at six mass balance sites: (a) Baltimore, (b) Pittsburgh, (c) Quebec 1, (d) Quebec 2, (e) Seattle, and (f) Tuk. Note that the record length for each site is different. The vertical range of temperature measurements is limited to the length of the thermistor string (i.e., -3 – -4 m to 1 m). The white lines indicate the snow surface and the base of the ice as recorded by different gauges at each site. When the snow depth equals zero, the elevation of the snow surface and the snow-ice interface are identical and define the ice surface. Depth is measured relative to the initial snow-ice interface; when surface melt starts, the ice surface is ablated below $z = 0$. Note that the vertical scale for Tuk is different.

Incident radiation showed little spatial variability and surface air temperatures were within 1° – 2°C at various locations within several km [Claffey et al., 1999; Perovich and Elder, 2001]. The snow and sea ice cover, on the other hand, is much more variable and spatially heterogeneous

(see Perovich et al. [2001, 2002b] and Sturm et al. [2002a] for a detailed description). This adds uncertainty in the proper definition of the snow thickness at the exact location of temperature measurements (discussed in more detail in section 3.2).

Table 1. Some Statistics of the Snow and Ice Thickness Measurements at the Pittsburgh Site^a

Gauge	h_{ini}	h_{fin}	h_{max}	h_{avg}	H_{ini}	H_{fin}	H_{max}	H_{avg}	g_{b}	m_{b}	m_{s}
053	0.05	0.26	0.33	0.22	2.26	1.58	2.78	2.38	0.52	0.43	0.77
069	0.06	0.12	0.45	0.26	1.70	1.37	2.40	2.02	0.70	0.43	0.60
071	0.05	0.07	0.24	0.14	2.13	1.68	2.78	2.38	0.65	0.34	0.76
Avg	0.05	0.15	0.31	0.21	2.03	1.54	2.65	2.26	0.62	0.40	0.71
BE	0.10	0.15	0.45	0.32	1.94	1.50	2.53	2.19	0.59	0.43	0.60
h_{p}	0.05		0.39	0.21							

^aExpressed in meters. The quantities h_{ini} , h_{fin} , h_{max} , and h_{avg} are the initial, final, maximum, and mean (winter) snow thickness, respectively. H_{ini} , H_{fin} , H_{max} , and H_{avg} are the initial, final, maximum, and mean ice thickness, respectively. Variable g_{b} is the total basal ice growth, m_{b} is the total basal ice melt, and m_{s} is the total surface ice melt. The initial thickness is that of 31 October 1997. The minimum snow thickness h_{min} is zero and is not included here. The minimum ice thickness H_{min} is equal to H_{fin} in all cases. “Avg” is the mean of the three thickness gauges, “BE” is the best estimates of the various quantities (see sections 3.1 and 3.2), and h_{p} is the snow depth derived from precipitation rates (which were multiplied by a factor of 1.5 as proposed by SIMIP2).

[23] *Perovich and Elder* [2001] present a more detailed description of the measurement methods, a summary of the mass balance measurements, and an analysis of the temporal evolution of the internal ice temperatures at various sites. A comprehensive description of the instrumental setup and the snow/ice data sets is provided by *Perovich et al.* [1999b]. The evolution of the snow and ice characteristics over the annual cycle at SHEBA are described in more detail by *Perovich et al.* [2001], *Perovich and Elder* [2001], *Perovich et al.* [2002b], and *Sturm et al.* [2002a]. Sea ice mass balance measurements at SHEBA are also documented by *Perovich et al.* [2003]. This work focuses on the examination of the Pittsburgh site, but also presents analyses for other sites for generality purposes.

3. Results and Discussion

[24] In this section, all available SHEBA data at the Pittsburgh site are analyzed in an attempt to construct a consistent data set for the temporal evolution of the snow depth, ice thickness, internal temperature, and ocean heat flux. These corrected data together with snow thermal conductivity derived from internal temperature measurements will be used to calculate a heat balance at the snow/ice surface (section 4) and ice base (section 5). These heat balances will also provide another measure of the self-consistency of the data set.

[25] There were five mass balance gauges at Pittsburgh. However, two of them were operational for a very short time, and consequently only the remaining three covering the whole measuring campaign (gauges 53, 69, and 71) are considered. Measurements made within just a few meters at the same site showed the same general temporal evolution, although substantial variations in actual thickness are present. For instance, the observed total ice surface melt at Pittsburgh ranged from 0.60 to 0.77 m, and from 0.50 to 1.00 m when considering all SHEBA sites [*Perovich et al.*, 2001].

[26] The initial, final and maximum snow and ice thicknesses, and the mean snow thicknesses for the selected gauges are listed in Table 1. The snow thickness increased during winter to reach a maximum in mid-May, a few days before surface melt started on 29 May. The maximum ice thickness, on the other hand, was reached a few days later at the beginning of June. On 29 May, a rainfall occurred, the surface turned gray, changing the albedo, and marking the onset of melting [*Perovich et al.*, 1999a]. The surface melt

of the ice, on the other hand, began when the snow cover completely disappeared in mid-June. Basal melt of the ice started in the second week of June when solar radiation warmed up the surface waters in leads and through the ice.

[27] At Pittsburgh, the mean winter snow thickness measured at gauges 53, 69, and 71 differs by 12 cm with a maximum daily difference between any two gauges of 34 cm. At the same three gauges, the mean ice draft differs by up to 36 cm with maximum differences equal to 56 cm. When comparing snow thickness measurements from different mass balance sites (several hundreds of meters apart), differences of 32 cm in mean winter snow thickness are observed with maximum daily differences of 70 cm.

[28] This variability in snow and ice thickness measurements shows that point measurements cannot be considered representative of the mean snow or ice thickness even on scales of a few meters. Since the mass balance gauges are typically a few meters away from the thermistor string, individual thickness measurements are not always representative of the thickness at the thermistor string. This is seen at all sites (Figure 2) where the individual stake measurements are plotted together with the internal temperature profile evolution. For instance, the ice base is often located at a depth where the internal ice temperature is much colder than the ocean freezing point or well within the mixed layer. This point is not only important for the computation of the energy budget (e.g., calculation of conductive heat flux), but also for the validation of thermodynamic sea ice models against SHEBA data.

3.1. Ice Thickness Evolution

[29] The snow and ice thickness at the thermistor string location can be determined from an analysis of the internal temperature profiles following the method of *Perovich and Elder* [2001]. This method works well when sharp changes in gradient are present at the snow/ice surface and ice base, but can give ambiguous results (1) when large and sudden changes in surface forcing occur (and the internal temperature profile is still responding to the change) and (2) during summer when the air temperature is close to 0°C resulting in almost isothermal snow or ice. Another limitation of this approach (particularly for the snow which sees the largest changes in surface forcing) is the low vertical resolution of the thermistor strings (typically 10 cm).

[30] At Pittsburgh, the internal temperatures for the ice base from gauges 53 and 71 are well within the isothermal part of the record (i.e., the ocean mixed layer), and those for

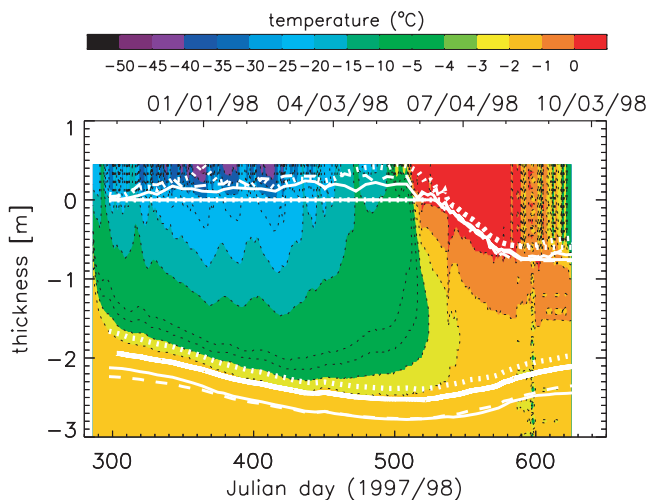


Figure 3. Thermistor string internal temperatures and measured snow-ice thickness evolution at Pittsburgh from gauges 71 (solid line), 69 (dotted line), and 53 (dashed line). For each gauge the elevations of the snow surface, ice surface, and ice base are shown using the same line style. The vertical extent of the temperature measurements is defined by the length of the thermistor string. The snow-ice interface in winter is at $z = 0$. When surface melt starts, the ice surface is ablated below $z = 0$. The bold white line represents the best estimate of the ice base evolution.

the ice base from gauge 69 are within the ice where temperature is colder than the ocean freezing point. However, individual ice thickness profiles at Pittsburgh (and at all other sites) have very similar shape, indicating that local differences in snow and ice thickness do not markedly affect the temporal evolution of the basal ice thickness. In the following, we take advantage of this fact and apply a constant vertical offset to the mean of the observed basal thickness time series of gauges 53, 69, and 71, such that the ice temperature at the ice base matches best the ocean freezing point temperature. This eliminates the difficulty associated with the determination of the summer ice thickness when the thermal gradients in the ice are very small.

[31] The accuracy of such a method is ± 5 cm (determined from the thermistor string resolution). The thickness curve obtained following this procedure is shown in Figure 3 along with individual measurements. Key characteristics of this inferred basal ice thickness evolution are given in Table 1 (referred to as the best estimate (BE)).

3.2. Snow Thickness Evolution

[32] The determination of the local snow depth at the thermistor string is more difficult, since all individual measurements show very different time evolutions. Several possibilities were considered in the following. The first option is simply to use the mean snow thickness of gauges 53, 69, 71 (Figure 4). An alternative way is to infer the snow thickness from the measured skin temperature and the internal temperature profiles. This is possible for monotonically increasing or decreasing internal temperature profiles, when the depth is a single valued function of snow temperature (provided the prescribed skin temperature is within the range of the thermistor string temperatures). In

this approach, the snow surface temperature is assumed to be equal to the skin temperature. At Pittsburgh, the skin temperature was not measured and instead the mean from four other sites was used. This is considered adequate, since the spatial variability in skin temperature is very small. The snow thickness at Pittsburgh derived from the measured skin temperatures is shown in Figure 4.

[33] Another option is to derive the snow depth from changes in the internal temperature gradient often present at the snow-air interface (“gradient method” [Perovich and Elder, 2001]). In this method, only internal temperature profiles that have reached steady state (i.e., when the air temperature remained constant to within a couple of degrees for 2 days) are used to ensure that the gradient change is in fact at the snow-air interface (Figure 4, white line).

[34] Finally, SIMIP2 proposes to use a constant snow density of 330 kg m^{-3} to convert observed precipitation rates into snow thickness. This simple approach ignores processes such as surface snow sublimation, blowing snow [Déry and Tremblay, 2004], compaction, and variation in fresh snow density as a function of temperature and wind [Colbeck, 1997; Déry and Yau, 2002]. This method results in a relatively thin snow cover compared to the stake measurements throughout most of the year. To account for the mismatch, SIMIP2 proposes to increase measured precipitation rates by 50% (Figure 4, dashed line). It is seen from Figure 4 that snow thicknesses reconstructed from the skin temperatures and gradient method agree well with one

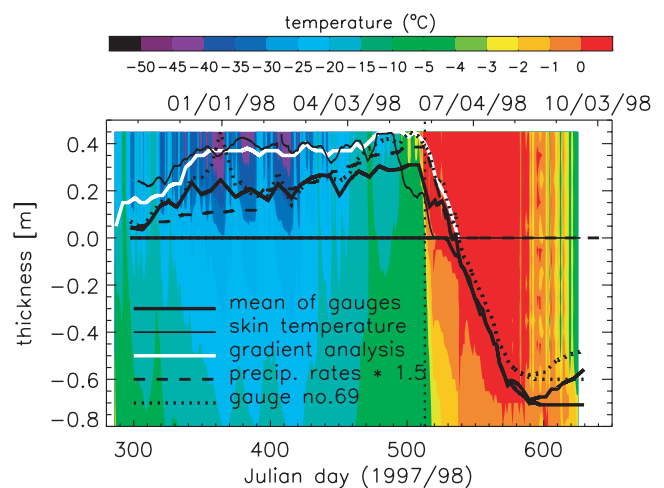


Figure 4. Snow surface elevation at the Pittsburgh site derived from various methods: mean of gauges 53, 69, and 71, skin temperature, gradient analysis, measured precipitation rates (assuming a reference snow density and applying a correction factor of 1.5 as proposed in SIMIP2), and gauge 69. Until mid-June (Julian day 530), the snow-ice interface for all three gauges are colocated (bold horizontal solid line). At the beginning of the following fall (Julian day 590) the bold solid and dotted lines represent the mean snow-ice interface elevation and that of gauge 69. Note that the gradient and skin temperature method cannot be used during summer. The vertical dotted line shows the observed onset of surface melt (29 May). Internal snow and ice temperatures are shown in the background.

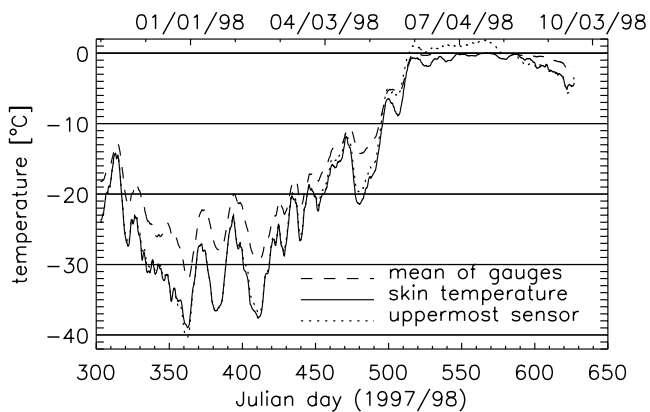


Figure 5. Thermistor string temperature at the elevation of the mean snow surface defined from Pittsburgh gauges 53, 69, and 71, skin temperature derived from radiometer measurements, and temperature of the uppermost sensor of the thermistor string (45 cm level). Temperatures are smoothed using a 7 day running mean.

another but are significantly different from the mean measured thickness and that derived from precipitation rates.

[35] Alternatively, the thermistor string temperature interpolated at a given snow surface elevation can be compared with skin or near-surface temperature to assess the representativeness of a given snow depth reconstruction. Figure 5 shows the thermistor string temperature at the elevation of the mean snow surface. As seen from this figure, these temperatures are significantly higher than the skin and near-surface air temperatures for most of the winter indicating that the mean snow depth underestimates the true snow depth. The uppermost thermistor reading (45 cm) is considered a near-surface air temperature, since the maximum snow thickness of all three gauges is always lower than 45 cm. Differences between this temperature and the temperature at the mean snow surface are largest (up to 7°C) during the three cold spells in winter, clearly showing that the temperature plotted is within the snow pack. In spring and summer, the temperature measured at the uppermost sensor is higher than the skin temperature presumably due to radiative heating of the thermistors and conduction down the plastic probe (compare section 2). In the following, the snow depth reconstructed from the gradient method is considered the most reliable during the winter (identified as BE in Table 1).

[36] The thickness of the snow cover at the end of the winter season has a large influence on the onset of surface ice melt and therefore on the total amount of surface melt during the summer season. This can be seen from Figure 4 and Table 1, where the difference between surface ice ablation at gauge 69 (thickest snow cover at the end of winter) and the mean of gauges 53, 69, and 71 is 11 cm. The difference in surface ice ablation between gauge 69 and 71 (thickest and thinnest snow cover at the end of winter) amounts to 16 cm (Table 1).

[37] Since the maximum snow depth from gauge 69 is very similar to the snow depth derived from the gradient method at the end of winter (see Figure 4), the surface evolution of gauge 69 is taken as the best estimate during the summer when the gradient method is no longer appli-

cable. *Jordan et al.* [2003] determined a very similar snow depth for Pittsburgh using profiles of the internal snow temperature. Some key statistics of the best estimate snow cover and ice surface (BE) are given at the end of Table 1. The error on the BE surface (Figure 4) is ± 5 cm (the vertical resolution of the thermistor string). Despite this error, the snow depth derived using this method is believed to be more realistic than the average of the three gauges.

3.3. Surface Conductive Heat Flux

[38] In situ needle probe measurements of the snow thermal conductivity at SHEBA gave an average value of $0.14 \text{ Wm}^{-1} \text{ K}^{-1}$ and a bulk density of 320 kg m^{-3} considering all SHEBA sites [*Sturm et al.*, 2001, 2002a]. These values are not in line with most published empirical equations relating conductivity and density [*Sturm et al.*, 1997]. (A snow thermal conductivity of $0.31 \text{ Wm}^{-1} \text{ K}^{-1}$ corresponds to a bulk density of about 330 kg m^{-3} , according to many conductivity-density relations.) Moreover, this value of $0.14 \text{ Wm}^{-1} \text{ K}^{-1}$ is a factor of 2 lower than the value commonly used in current sea ice models ($0.31 \text{ Wm}^{-1} \text{ K}^{-1}$ (C. M. Bitz and G. A. Schmidt, personal communication, 2004)), and also proposed by SIMIP2.

[39] In the study of *Sturm et al.* [2002b] it is shown that the in situ value of $0.14 \text{ Wm}^{-1} \text{ K}^{-1}$ is not consistent with observations of basal ice accretion during the winter. Instead, they infer a bulk snow thermal conductivity of $0.33 \text{ Wm}^{-1} \text{ K}^{-1}$ derived from observed snow depth, air and snow-ice interface temperatures, basal ice growth, and the ocean heat flux. In the following, it is shown that an even larger value is necessary to satisfy the continuity of heat flux condition at the snow-ice interface at SHEBA.

[40] In contrast to pure thermal conduction in a solid body, latent heat transport associated with water vapor diffusion (driven by the temperature and therefore specific humidity gradient from the snow base to the snow surface) and advective heat transport associated with wind pumping, also take place in a snow layer. The resulting total heat transport is often referred to as the effective conductive heat flux which can be much higher than the transport of heat by thermal conduction alone. Those processes are neglected in most thermodynamic sea ice models, and consequently a larger value of snow thermal conductivity should be used in those models. From the SHEBA internal snow and ice temperature data, and assuming the ice conductivity to be known, an effective thermal conductivity of snow can be calculated.

[41] Figure 6 shows the conductive heat fluxes at the ice base, ice surface, snow base and snow surface (best estimate) using ice and snow conductivities of $2.03 \text{ Wm}^{-1} \text{ K}^{-1}$ and $0.31 \text{ Wm}^{-1} \text{ K}^{-1}$ respectively. During winter, the temperature gradients at the snow-ice interface are calculated using second-order one-sided differences. At the snow surface and the ice base, temperature gradients are approximated using linear differences between two temperature points (within the snow or ice), 15 cm apart in the snow, and 40 cm apart in the ice, since the snow surface and the ice base are not represented by thermistors. Linear approximations are also used to calculate the temperature gradients at the snow-ice interface when the snow thickness is smaller than 15 cm (distance between first and third thermistor used in the second-order scheme) or when the ice surface starts to

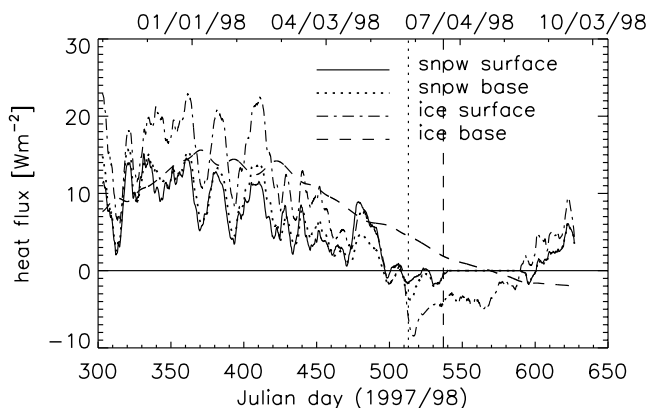


Figure 6. Conductive heat flux at the ice base, ice surface, snow base, and snow surface. Fluxes are smoothed using a 7 day running mean. Dotted and dashed lines denote the onset of snow and ice surface melt (29 May and 21 June, respectively). In this figure, only the conductive heat flux at the ice base is defined as positive upward to ease comparison.

melt and the ice surface is no longer represented by a thermistor.

[42] The basal conductive heat flux is damped and lags the snow or ice surface conductive heat flux by approxi-

mately 15 days in winter, owing to the heat storage in the ice. For the same reason, the conductive flux at the ice surface has an opposite sign than at the base during summer between Julian days 510 and 590, when heat is conducted from above and below toward the inner part of the ice layer. At the end of summer (Julian days 570–630), the basal conductive heat flux changes sign as the ice base is at the ocean freezing point temperature (below zero) and the ice surface is at 0°C , resulting in a downward heat flux.

[43] Figure 6 shows that a large discrepancy exists between the snow and ice conductive heat fluxes at the snow-ice interface during winter, when using a snow conductivity of $0.31 \text{ Wm}^{-1} \text{ K}^{-1}$. Assuming continuity of heat fluxes at the snow-ice interface ($-k_s \nabla T_s = -k_i \nabla T_i$, where k_s and k_i are the thermal conductivities of snow and ice, and T_s and T_i are the snow and ice temperatures), k_s can be calculated from the internal temperature profiles assuming a value of k_i (equal to $2.03 \text{ Wm}^{-1} \text{ K}^{-1}$, in accord with surface ice observations from the Beaufort Sea [Perovich *et al.*, 1997]). To reduce the effects of penetrating shortwave radiation, only times with no or low solar radiation are considered. To calculate the snow thermal conductivity, temperature gradients on both sides of the snow-ice interface are approximated with second-order one-sided difference scheme. Both Quebec 2 and Tuk were excluded from this analysis, since the snow cover (5–10 cm) was too thin to provide reliable temperature gradient estimates.

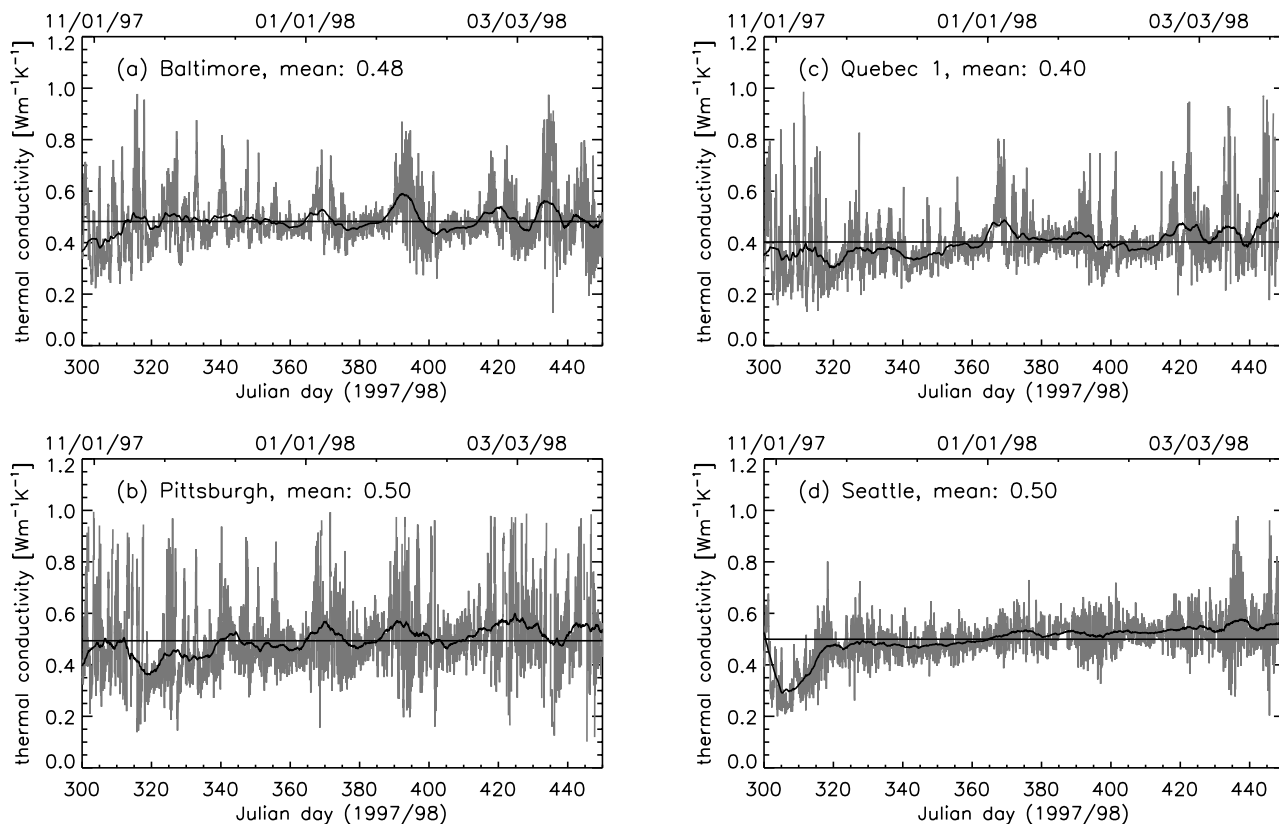


Figure 7. Snow thermal conductivities calculated from observed internal temperature profiles at (a) Baltimore, (b) Pittsburgh, (c) Quebec 1, and (d) Seattle. Only times when the penetrating shortwave radiation is small are considered. Hourly values are shown with a solid line. The bold line is a 7 day running mean, and the horizontal line represents the mean. A value of $2.03 \text{ Wm}^{-1} \text{ K}^{-1}$ was used for the ice thermal conductivity.

[44] Figure 7 shows that snow conductivities range from 0.40 to 0.50 $\text{Wm}^{-1} \text{K}^{-1}$ for the sites Baltimore, Pittsburgh, Quebec 1, and Seattle with a mean of 0.47 $\text{Wm}^{-1} \text{K}^{-1}$. The snow thermal conductivity for the Pittsburgh site is equal to 0.50 $\text{Wm}^{-1} \text{K}^{-1}$. This value would correspond to a mean snow density in the range of 400 to 550 kg m^{-3} (using different density-conductivity relations [Sturm *et al.*, 1997]) if other heat transport mechanisms such as latent heat transport associated with water vapor diffusion or wind pumping were ignored. Note that the value for the snow thermal conductivity calculated from the conductive heat fluxes at the snow-ice interface is sensitive to the order and the Δz used in the approximation of the snow or ice temperature gradients. Various combinations of linear and second-order approximations result in mean values ranging from 0.50 to 0.68 $\text{Wm}^{-1} \text{K}^{-1}$ for the Pittsburgh site. In general, second-order schemes lead to lower mean values than linear schemes, and the time series are less noisy.

[45] The low-frequency variability (30 days) in the conductivity time series appears to be linked with inaccuracies in the temperature gradient estimates associated with the low vertical resolution of temperature measurements. This can be seen in Figure 7b, where peaks in the thermal conductivity (e.g., Julian days 370 and 390) correspond with peaks in air temperatures (Figure 1a). In fact, the warming of the surface combined with the low vertical resolution of internal temperature in the snow (resolution is the same as that of the ice, yet it is subjected to higher-frequency forcing, it is thinner, and has lower heat capacity) results in an underestimation of the temperature gradient at the snow base and a large inferred effective snow conductivity. The high-frequency scatter in the derived conductivities is presumably due to errors associated with taking derivatives of a discretized temperature signal.

[46] Spatial variability in snow depth and inhomogeneities of the ice thickness result in local horizontal temperature gradients and heat transports. These will lead to some errors in the effective thermal conductivities of snow, derived from internal temperature profiles assuming strictly one-dimensional heat conduction (as was done above). At Pittsburgh, thickness gauges were at least 1 m apart from one another. The winter snow thickness measured at gauges 53, 69, and 71 shows a mean maximum daily difference between any two gauges of 14 cm, and a maximum difference of 34 cm with a standard deviation of 7 cm.

[47] To assess the error associated with two-dimensional effects, a 2-D steady state heat conduction model was run with specified ocean and air temperature, and with a specified spatially varying snow depth at the surface. The simulated vertical temperature profiles are then used to calculate the snow thermal conductivity (assuming continuity of heat fluxes at the snow-ice interface) at each x location in the model domain. These values are then compared to the snow thermal conductivity used in the 2-D model to assess the error. Results from this model (not presented here) show that a 14 cm snow thickness change (from 20 cm to 34 cm) over a distance of 1 m results in an error of $\pm 12\%$ in the snow thermal conductivity (using a k_s value of 0.31 $\text{Wm}^{-1} \text{K}^{-1}$ in the model). When using a snow thickness change equal to the mean plus one standard deviation (14 + 7 cm), the error is 18%.

[48] It is interesting to note that this error is independent of air temperature, and is only slightly sensitive to the mean snow cover thickness. A higher snow thermal conductivity as implied by the SHEBA data analysis would make this error even smaller. Finally, this error is both positive and negative (with almost zero mean) depending whether the vertical temperature profile is located on the deep or shallow half of the surface snow depth change. From these results, the snow thermal conductivity inferred at Pittsburgh (0.50 $\text{Wm}^{-1} \text{K}^{-1}$) can be under- or overestimated by $\pm 0.06 \text{Wm}^{-1} \text{K}^{-1}$ (or up to 0.09 $\text{Wm}^{-1} \text{K}^{-1}$ using the mean error plus one standard deviation), in accord with the 7 day average variability in the snow thermal conductivity shown in Figure 7.

[49] At Pittsburgh, given that the mean snow depth at the thermistor site is almost twice that of the 3 surrounding thickness gauges, the snow possibly loses some heat horizontally and the snow thermal conductivity inferred from the continuity of the conductive heat flux at the snow ice interface would be slightly overestimated. However, similar values for k_s were obtained for the sites Baltimore, Quebec 1 and Seattle where the snow thickness at the location of the thermistor string is not always larger than the surrounding gauges (e.g., Quebec 1, Seattle).

[50] The annual means of the conductive heat fluxes at the ice base and ice surface are 7.1 Wm^{-2} and 7.2 Wm^{-2} in contrast with 4.3 Wm^{-2} at the snow or ice surface (ice surface considered when snow is absent) for a snow thermal conductivity of 0.31 $\text{Wm}^{-1} \text{K}^{-1}$. Using a snow thermal conductivity of 0.50 $\text{Wm}^{-1} \text{K}^{-1}$ derived for the Pittsburgh site gives a mean conductive heat flux at the snow or ice surface of 7.2 Wm^{-2} , in agreement with the ice conductive fluxes (see Table 2).

4. Surface Energy Budget

[51] A surface energy budget at SHEBA calculated from measurements of the radiative fluxes (including the albedo), atmospheric turbulent heat fluxes (computed from standard bulk formulations), the energy of melt (inferred from changes in snow/ice thickness) and the conductive heat flux (inferred from internal temperature profiles) is presented as a test of consistency for the corrections proposed in the previous section.

[52] The budget can be written as (fluxes toward the surface are defined positive)

$$(1 - \alpha)(1 - i_0)F_{\text{swd}} + F_{\text{lwd}} + F_{\text{lwu}} + F_{\text{sh}} + F_{\text{lh}} + F_{\text{cs}} + F_{\text{ms}} = 0, \quad (1)$$

where α is the albedo, i_0 is the fraction of net shortwave radiation penetrating into the interior of the snow or ice, F_{swd} is the downward shortwave radiation, F_{lwd} and F_{lwu} are the downward and upward longwave radiation, F_{sh} and F_{lh} are the sensible and latent heat flux, F_{cs} is the effective conductive heat flux at the surface, and F_{ms} is the heat absorbed associated with surface melting (referred to as the energy of melt). The salinity of the ice surface is assumed to be equal to zero (due to brine percolation). Accordingly, the specific latent heat of fusion for zero salinity is used in the computation of the energy of melt.

Table 2. Monthly and Yearly Means of the Energy Budget Components^a

Variable	Nov.	Dec.	Jan.	Feb.	March	April	May	June	July	Aug.	Sept.	Oct.	Year Mean
F_{swd}	0.1	0.0	0.0	5.1	46.3	142.3	248.7	280.4	211.4	110.8	39.9	20.0	92.1
F_{swu}	-0.1	0.0	0.0	-4.3	-39.4	-120.5	-204.4	-200.2	-135.9	-77.6	-25.9	-13.0	-68.5
F_{sw}	0.0	0.0	0.0	0.8	7.0	21.9	44.4	80.1	75.5	33.2	13.9	7.0	23.6
F_{swp}	0.0	0.0	0.0	0.1	0.6	1.8	3.6	9.6	12.8	5.5	0.5	0.2	2.9
F_{ldw}	209.6	152.0	170.5	163.8	201.2	220.0	245.7	282.5	299.7	299.3	282.2	245.9	231.0
F_{ldu}	-227.1	-185.2	-197.6	-190.2	-222.1	-242.4	-273.7	-308.2	-314.5	-310.7	-293.0	-260.1	-252.1
F_{lw}	-17.6	-33.2	-27.1	-26.4	-20.8	-22.4	-28.0	-25.7	-14.8	-11.4	-10.7	-14.2	-21.0
F_{sh}	3.4	6.4	4.7	7.5	3.0	0.6	-1.1	1.5	1.6	-2.3	-0.4	1.5	2.4
F_{lh}	0.3	0.3	0.1	0.0	-0.6	-0.5	-2.1	-2.2	-0.3	-1.5	-0.9	-0.3	-0.6
F_{net}	-13.8	-26.5	-22.4	-18.2	-12.0	-2.1	11.9	44.2	49.1	12.5	3.8	-5.0	1.7
F_{cs}	14.8	19.7	13.1	13.1	8.3	7.0	2.2	-2.0	-3.7	-0.5	4.6	9.7	7.2
F_{ms}	0.0	0.0	0.0	0.0	0.0	0.0	-3.2	-30.4	-48.0	-6.0	-4.0	-2.0	-7.8
F_{rs}	1.0	-6.8	-9.3	-5.2	-3.7	4.8	10.9	12.4	-2.7	7.6	5.4	3.2	1.5
F_{cb}	-9.4	-13.0	-14.6	-13.3	-11.9	-8.2	-5.5	-2.6	-0.4	1.3	-2.3	-5.9	-7.1
F_{mb}	6.4	9.6	10.7	8.3	4.5	4.2	0.9	-7.3	-13.5	-15.2	-8.0	-0.8	0.0
F_{ocn}	3.0	3.4	3.9	5.0	7.4	4.0	4.6	9.9	13.9	13.9	10.3	6.7	7.1

^aAbbreviations are as follows: F_{swd} , F_{swu} , F_{sw} , F_{swp} , downward, upward, net, and penetrating shortwave radiation, respectively; F_{ldw} , F_{ldu} , F_{lw} , downward, upward, and net longwave radiation, respectively; F_{sh} , F_{lh} , sensible and latent heat flux, respectively; F_{net} , net atmospheric heat fluxes; F_{cs} , conductive heat flux at the surface; F_{ms} , energy of melt at the surface; F_{rs} , net residual heat flux at the surface. The last three lines show the monthly and yearly means of the basal conductive heat flux (F_{cb}), energy of melt (F_{mb}), and the net residual heat flux, i.e., the ocean heat flux (F_{ocn}). All values are given in Wm^{-2} .

[53] In the budget of surface fluxes (Figure 8), the albedo and the radiative fluxes are measured directly while the turbulent fluxes, the energy of melt, and the conductive heat flux in the snow and ice are inferred from other measured quantities. Surface ice thickness measurements which showed an increase in the summer were ignored in the surface evolution time series. This eliminated a few positive spikes in the energy of melt curve. Following the analysis presented in section 3.3, the conductive heat flux in the budget is computed using a snow thermal conductivity of $0.50 \text{ Wm}^{-1} \text{ K}^{-1}$ determined at the Pittsburgh site, and considering the best estimates of ice base and snow surface described in sections 3.1 and 3.2. In the budget, the fraction of net shortwave radiation penetrating the surface (i_0) is set equal to 0.17 and 0.08 for ice and snow, respectively. The value of i_0 for ice is in general agreement with the value used in other modeling studies [e.g., *Ebert and Curry, 1993; Flato and Brown, 1996*], whereas that of snow is based on energy flux measurements of an Arctic tundra snow cover presented by *Ohmura [1984]* (in contrast with other studies which use a value of zero).

[54] Figure 8a shows how the conductive heat flux in winter (October–March) is controlled by the net longwave radiation. The net longwave radiation has large variability. It is generally high for clear sky conditions, and low for cloudy sky, and constitutes a heat loss from the surface throughout the whole year. The net shortwave radiation (Figure 8a) is steadily growing in spring and early summer with a sudden increase in mid-June when the snow cover starts disappearing and the albedo drops to a lower value. When the surface temperature is at the melting point, the energy surplus is used for melting. This heat flux becomes the major counterbalance of the net solar flux during summer (April–September).

[55] The sensible heat flux (Figure 8b) is usually small except in winter during clear sky conditions when the air temperature is relatively higher than the surface and the wind speed is higher [see *Walsh and Chapman, 1998*] (see Figure 1). In general, the surface is colder than the overlying air and the sensible heat is downward. During the winter,

the sensible heat flux and the net longwave radiation are generally anticorrelated (Figures 8a–8b). That is, the heat loss from the surface to the atmosphere during clear sky conditions leads to a positive temperature gradient in the air

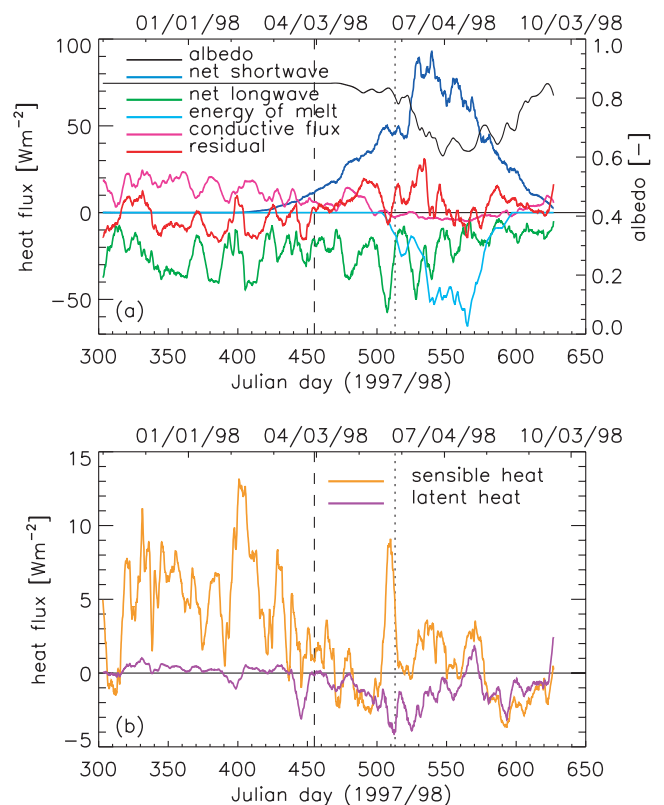


Figure 8. (a) Main components of the Surface Heat Budget of the Arctic Ocean (SHEBA) surface energy budget at the Pittsburgh site. (b) Sensible and latent heat fluxes (calculated using bulk formulations). The dashed line indicates the beginning of the summer (1 April), and the dotted line marks the onset of surface melt (29 May). Fluxes are smoothed using a 7 day running mean.

and results in a downward sensible heat flux. The coupling between these two fluxes is discussed in more detail by *Makhtas et al.* [1999]. The latent heat flux (Figure 8b) is close to zero except after the onset of the melt season when it has several peaks indicating moisture transport from the surface to the atmosphere. Figure 8a shows most components of the surface energy budget together, and the residual from all fluxes.

[56] Annual means for all components of the energy budget are calculated from monthly mean components and are given in Table 2. The radiative fluxes for the month of October 1998 are linearly interpolated from the September 1998 and November 1997 means following [*Persson et al.*, 2002]. For the remaining components of the energy budget, monthly mean values for September and October are linearly interpolated from the August 1998 and November 1997 means. (Note that the measurements of the internal snow/ice temperature at Pittsburgh, and the skin temperature are only available from 31 October 1997 to 20 September 1998.)

[57] In the surface heat budget, the sum of all atmospheric fluxes should be balanced by the surface conductive flux and/or surface melt. This is not always the case at the Pittsburgh site where conduction at the surface during winter only partly balances the net atmospheric flux. This imbalance in winter amounts to a mean energy deficit of 3.5 Wm^{-2} at the surface. The discrepancy at the surface is presumably due to poorly defined thermal gradients associated with the coarse resolution of the thermistors in the snow, small errors associated with radiative heating of the thermistors during summer, and conduction of heat in the polyvinyl-chloride rod.

[58] During summer, a mean surplus of 6.4 Wm^{-2} is observed which mainly results from an imbalance of the atmospheric net radiative flux and the energy of melt at the surface (e.g., in early June, Julian days 510–530). Uncertainty in the magnitude of the energy of melt associated with errors in snow/ice surface elevations may explain the imbalance present during the warm season. Snowfall during the melt period is not considered. The computed energy of melt accounts for both ice and snow melt. The annual mean of the energy of melt (7.8 Wm^{-2}) corresponds to the observed 60 cm of surface ice melt, and 45 cm of snow melt at a reference density of 330 kg m^{-3} (equivalent to a 16 cm surface ice melt).

[59] The yearly mean error in the budget is small (1.5 Wm^{-2}). This is fortuitous however, as it is the result of a sizable mean energy deficit in winter and a sizable mean surplus in summer. The net imbalances in winter are mainly due to errors in the net longwave radiation and conductive heat flux, whereas the imbalances in the summer are a result of errors in the net shortwave radiation and energy of melt. There are considerable discrepancies between radiative flux measurements at the ASFG and the SPO towers [*Persson et al.*, 2002] (hereinafter referred to as P02). For instance, the hourly measurements of incoming longwave radiation at the two tower sites show a mean and root-mean-square difference of 3 Wm^{-2} and 4.6 Wm^{-2} for the period of December 1997 through September 1998. Differences are even larger for incoming shortwave radiation (7.7 Wm^{-2} mean and 11.1 Wm^{-2} root-mean-square difference) for the period from March 1998 through September 1998. P02 estimate the

accuracy of the absolute bias in the longwave components measured by the ASFG to be $\pm 2.5 \text{ Wm}^{-2}$, and the uncertainty in downward shortwave radiation to be $\pm 3\%$. Nevertheless, the budget is considered to close taking into account errors associated with the radiative flux measurements, uncertainties in snow and ice depth, and in snow thermal conductivity estimates.

[60] In this budget, the energy of melt is calculated from thickness changes and thus constitutes an independently evaluated component of the surface energy budget. This way, it is possible to evaluate the net imbalance (the residual of all fluxes) of the surface energy budget. This is in contrast with P02, where the integrated excess energy (the residual component) in the budget is set equal to the observed total surface ablation. In general, calculated values of the surface energy budget of this study agree well with a similar analysis by P02. Both budgets identify an energy deficit during winter and a surplus during summer. In this study, the fraction of net shortwave radiation which penetrates into the ice is taken into account in contrast with P02 (annual mean: 2.9 Wm^{-2} , see Table 2). Minor differences between the annual means of the turbulent heat fluxes are due to the different computation methods (bulk formulations here and eddy correlation in P02). The annual mean of the surface conductive flux (7.2 Wm^{-2}) is a factor of 1.4 larger than the corresponding value in P02, in loose agreement with the ratio of the snow thermal conductivities ($0.50/0.31 = 1.6$) used in the computation of these fluxes.

5. Basal Energy Budget

[61] The budget at the ice base includes the ocean heat flux (F_{ocn}), the conductive heat flux into the ice (F_{cb}) and the energy of melt (F_{mb}). Both F_{cb} and F_{mb} are derived indirectly from the internal ice temperature profiles and the basal growth and melt rates. The ocean heat flux used in the basal energy budget, on the other hand, is calculated as a residual following the approach of *Perovich and Elder* [2002] (also adopted in SIMIP2). Measured ocean heat fluxes derived from the covariance of temperature and vertical velocity component in the upper ocean, and ocean heat fluxes derived using a bulk formulation [*McPhee et al.*, 2003] will also be compared to check the consistency of this method.

[62] The basal heat budget (fluxes toward the surface are defined positive) can be written as

$$F_{\text{ocn}} + F_{\text{cb}} + F_{\text{mb}} = 0. \quad (2)$$

[63] To calculate the energy of melt, the salinity and temperature dependence of the latent heat of fusion is taken into account [*Bitz and Lipscomb*, 1999]. A value of 29.6 psu was used for the salinity of the upper ocean at SHEBA [*McPhee et al.*, 1998], corresponding to a freezing point temperature of -1.6°C . This value is in the range of the temperature measurements from the lowest thermistor on the string made during the SHEBA period (-1.4° to -1.8°C). The salinity at the ice base is considered equal to 4 psu in accord with salinity profiles measured at SHEBA [*Perovich and Elder*, 2002]. Newly formed ice usually has higher salinity but desalinizes quickly in the first few weeks

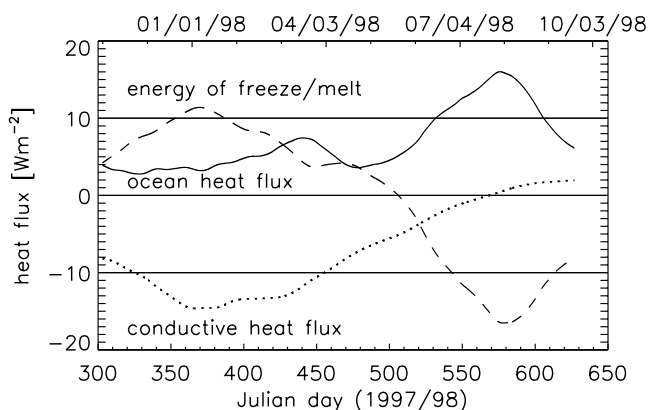


Figure 9. Components of the basal energy budget at the Pittsburgh site: ocean heat flux, conductive heat flux, and energy of freeze/melt. Fluxes are smoothed using a 30 day running mean.

[Cox and Weeks, 1988]. Here a salinity of 10 psu is assumed for newly formed ice and a salinity of 4 psu is assumed when basal melting occurs. A salinity of 4 psu (10 psu) results in a temperature- and salinity-dependent effective specific latent heat of fusion of $0.87 L_{f0}$ ($0.67 L_{f0}$), where L_{f0} is the specific latent heat of freshwater ice. Growth/melt rates are calculated from the ice thickness time series.

[64] To calculate the conductive heat flux at the ice base, the salinity- and temperature-dependent thermal conductivity of ice is used [Maykut and Untersteiner, 1971]. For a salinity of 4 psu, the ice conductivity value is $1.74 \text{ Wm}^{-1}\text{K}^{-1}$. (The ice conducting heat away from the base where ice is formed is assumed to have desalinated to 4 psu.) The conductive heat flux at the ice base is determined from a first-order approximation of the internal temperature gradient between the ice base and a level 40 cm above the base (see section 3.3). The heat associated with melting or freezing is computed from the rate of change in thickness at the ice base and the effective specific latent heat of fusion. The temporal resolution of the derived energy of melt is 2 days in summer and 2 weeks in winter in contrast to the hourly values of the conductive heat fluxes. For consistency, the energy of melt/freezing has been linearly interpolated to a 1 hour time step.

[65] Figure 9 shows the ocean heat flux, the basal conductive heat flux and the energy of melt/freezing. Their annual means are computed from the monthly mean components (where September and October means are linearly interpolated from the August 1998 and November 1997 values) and are equal to 7.1 Wm^{-2} , -7.1 Wm^{-2} and 0.0 Wm^{-2} , respectively (see Table 2). Note that the mean energy of melt/freezing is zero despite the fact that there is a net decrease in ice thickness during the SHEBA year. This is due to the fact that ice forms at a higher salinity and melts at a relatively lower salinity value.

[66] The annual mean ocean heat flux provided in SIMIP2 (see Figure 11) is 8.1 Wm^{-2} and would result in an imbalance if considered in the present basal energy budget. Differences between the SIMIP2 ocean heat flux and the value calculated here are presumably due to

different assumptions about the salinity- and temperature-dependent thermal conductivity of ice and the latent heat of fusion used in the heat budget. Also note that for model validation purposes, the same assumption about the salinity of newly formed ice and vertical salinity profile must be made in order to be consistent with the prescribed ocean heat flux. The basal energy budget closes exactly, as the ocean heat flux is derived as a residual of the other two components. This ocean heat flux will be compared to the measured ocean heat flux, to the ocean heat flux derived using a bulk formulation, and the ocean heat flux provided by SIMIP2 (see below).

[67] To get an estimate of the variability in ocean heat fluxes at SHEBA, it was calculated at five other mass balance sites where internal ice temperature was measured (Figure 10). The energy of melt and the conductive heat flux at the ice base are computed using the best estimates for the ice thickness at each site (see section 3.1). In the computation of the mean ocean heat flux (thick red line), some line intervals for certain mass balance sites were excluded (dotted lines in Figure 10). At Quebec 1, the ocean heat flux is ignored after Julian day 435, since there is a discontinuity in the internal temperature measurements (see Figure 2c). Tuk is excluded altogether as it is located on an old consolidated ridge where the ocean heat flux is expected to be larger and not representative for undeformed multiyear ice [Schramm et al., 2000]. The annual mean of the ocean heat flux for the 5 mass balance sites is 7.4 Wm^{-2} , slightly higher than the mean ocean heat flux at Pittsburgh (7.1 Wm^{-2}).

[68] Despite some differences between locations, the ocean heat fluxes show very similar patterns. From October to mid-January the ocean heat flux is often very small. The low ocean heat fluxes are due to the stratification of the mixed layer associated with the previous summer melt. This period is followed by a double peak in February and March. These two peaks in ocean heat flux are due to storm activity (compare wind speed in Figure 1e), entraining pycnocline water into the mixed layer, and also due to a change in

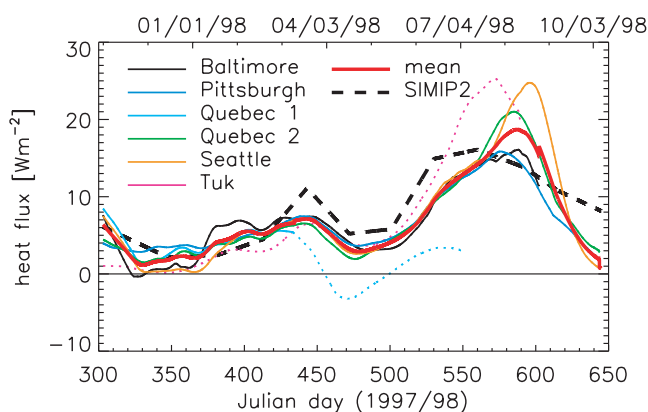


Figure 10. Ocean heat flux derived from growth/melt rates at the ice base and internal temperature from six SHEBA sites. The bold red line is the mean of all sites. Dotted lines indicate portions of the series that are ignored when the mean is computed. Fluxes are smoothed using a 30 day running mean.

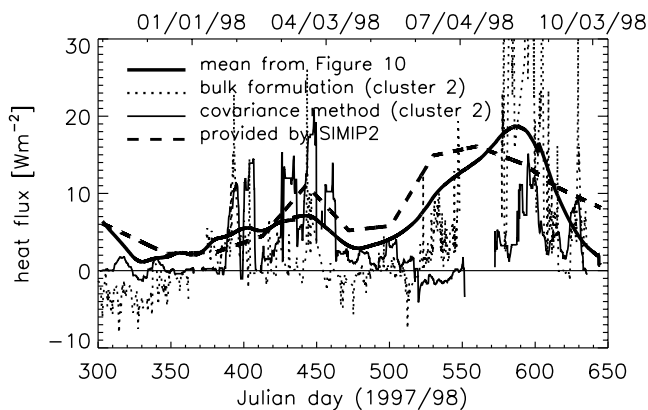


Figure 11. Mean ocean heat flux derived from the growth/melt rates presented in Figure 10, ocean heat flux derived from turbulence measurements (7 day running mean applied), ocean heat flux derived using a bulk formulation, and ocean heat flux provided in SIMIP2.

bathymetry, as the SHEBA camp was drifting over a region of shallower water [Perovich *et al.*, 1999a; Perovich and Elder, 2002] (75°N, 160°W). Beginning in May, the ocean heat flux starts to increase and reaches a maximum of about 16 Wm^{-2} in early August before it drops relatively fast to about 2 Wm^{-2} in early October. The large peak in summer is due to solar radiation which warms up the surface waters either through leads or through the ice [Maykut and McPhee, 1995]. While the ice concentration decreases, large amounts of shortwave radiation are absorbed by areas of open water (highly stratified due to the melting). This leads to lateral melt which further stabilizes the surface waters until wind increases and mixes the warm surface waters down, causing basal melt.

[69] In Figure 11, the mean ocean flux from five mass balance sites is compared to the ocean heat flux derived from turbulence measurements [McPhee, 2002], a bulk formulation [McPhee *et al.*, 2003], and from SIMIP2 [Perovich and Elder, 2002]. The turbulence data (3 hour temporal resolution) are smoothed using a 7 day running mean. No attempt is made to fill the gaps when no data are available. In general, the ocean heat flux computed using the bulk formulation, and those derived using the covariance method are in agreement, i.e., both show very small ocean heat fluxes from the beginning of November to mid-January. The mean ocean heat flux (from the residual method) is in reasonable agreement with the covariance ocean heat flux measurements. In particular, the two peaks in early spring (Julian days 400 and 450) and the summer peak are captured by both methods. In early winter (Julian days 300–380), and then later in June and July (Julian days 520–570), the ocean heat fluxes from turbulence measurements and from the bulk formulation are significantly lower than those from the residual method. The ocean heat fluxes derived with the residual method are on average larger but also show a minimum during that time (some mass balance sites do show zero ocean heat flux during this period however). The magnitude of the ocean heat flux determined with the residual method is a function of the assumed salinity of newly formed ice, and could account for the

discrepancy between ocean heat fluxes derived using other methods.

[70] The mean ocean heat flux inferred from the ice thickness and internal ice temperature is generally similar to the one provided in SIMIP2 until the end of February. Afterward it is significantly smaller (except in August where it is larger) although it was determined using the same method. The summer peak of the SIMIP2 curve has its maximum around Julian day 560, about one month earlier than the derived mean ocean heat flux. Differences in magnitude likely result from the definition of the ice base, the method of approximating temperature gradients at the base, and the assumption for the prescribed salinity profile and the salinity of newly formed ice.

[71] In early summer, when incident solar radiation is at maximum (Julian days 500–550), the heat flux at the turbulence mast remains small. This small ocean heat flux is a result of a significant input of solar radiation into the ocean mixed layer where it is distributed and eventually raises the mixed layer temperature above its freezing point. In ice-covered leads and below thin ice, the ocean mixed layer temperature reflects the diurnal cycle of solar radiation. The resulting warming of the upper ocean can temporarily lead to downward ocean heat fluxes of up to 70 Wm^{-2} [McPhee and Stanton, 1996]. In the Arctic, a major fraction of the sensible heat flux from the ocean to the ice originates from shortwave radiation absorbed in the upper ocean rather than from relatively warm waters below the mixed layer [Maykut and McPhee, 1995].

[72] The ocean heat flux is also influenced by the evolution of “false bottoms” between under ice melt ponds and the ocean mixed layer. The formation of false bottoms during the melt season occurs in many places in the Arctic and can have a significant thermodynamic influence on the energy budget at the sea ice base when latent heat is released to the ocean mixed layer [Notz *et al.*, 2003]. At SHEBA, false bottoms were observed at more than 10% of the thickness gauges [Eicken *et al.*, 2002; Perovich *et al.*, 2003]. The thermodynamic effects of false bottom formation during the ablation period (Julian days 510–590) are not captured by the residual method used to derive the ocean heat flux but might be evident in the ocean heat flux from the covariance method. Both the false bottom evolution and the input of solar radiation to the ocean mixed layer are likely reasons for the discrepancy between the ocean heat flux derived at the mass balance site and that from the turbulence measurements.

[73] The determination of the ocean heat flux from ice thickness and internal ice temperature measurements was also applied in previous investigations. In an earlier experiment, McPhee and Untersteiner [1982] derived the ocean heat flux from the temperature gradient and growth rate of sea ice. They found values for the ocean heat flux of less than 2 Wm^{-2} from March to May northwest of Spitsbergen in the Arctic Ocean (drifting ice station FRAM 1, 1979). Using ice thickness and temperature data measured during fall 1998 in the Arctic Ocean, Wettlaufer *et al.* [1990] determined a range of 0 to 37 Wm^{-2} for the oceanic heat flux, whereas Perovich *et al.* [1989] found even larger values ($7\text{--}128 \text{ Wm}^{-2}$) in the marginal ice zone in December. These values are about an order of magnitude

larger than ocean fluxes calculated in many ice-ocean models.

[74] According to *Wetlaufer* [1991], the oceanic heat flux is an important component of the sea ice energy and mass balance but is often horizontally very inhomogeneous and temporally variable. For an unmanned 15 months measuring deployment in the Beaufort Sea in 1993/94, *Perovich et al.* [1997] determined an annually averaged oceanic heat flux of 4 Wm^{-2} with a maximum average summer peak of 9 Wm^{-2} , when computed as a residual of the basal energy budget. They found the ocean heat flux during winter to be very close to zero. *Maykut and McPhee* [1995] inferred the ocean heat flux during AIDJEX from the upper ocean heat content and the turbulent friction velocity. The annual mean of 5.1 Wm^{-2} is in good agreement with the 1993/94 average of 4 Wm^{-2} determined in the Beaufort Sea. All these results show, that the ocean heat flux is very variable on different horizontal and temporal scales. In the present study, the annual mean ocean heat flux at Pittsburgh is 7.1 Wm^{-2} with early winter values around 3 Wm^{-2} . These are well within the range of previous observations.

6. Conclusions

[75] Sea ice models are usually forced with atmospheric and oceanic forcing fields and validated against ice thickness temporal evolutions. However, since large errors in the forcing data set can be present (e.g., precipitation, ocean heat fluxes), and since the correct ice thickness temporal evolution at a given point can be achieved in a number of ways (i.e., different combinations of snow depth, snow thermal conductivity, ocean heat flux can give the same ice thickness evolution), additional validation data sets are required to better constrain the problem. Data from the Surface Heat Budget of the Arctic Ocean (SHEBA) experiment constitute such a data set by providing many independent but related observations. These include precipitation, snow depth, ice thickness, internal snow/ice temperature and surface temperature from radiative measurements. However, these observations were not always made exactly at the same location (ranging from a few meters to several hundred meters). Since there is high variability in snow and ice thickness at small spatial scales, this leads to inconsistencies in the forcing and validation data sets.

[76] This paper presents a consistent forcing and validation data set for sea ice model validation purposes. The main goals of this paper are to analyze all data available for the Pittsburgh mass balance site (the official mass balance site for the Sea Ice Model Intercomparison Project, Part 2, Thermodynamics), identify inconsistencies between the various fields, and propose corrections for those same variables. A companion paper [*Huwald et al.*, 2005] presents a validation of a sigma-coordinate thermodynamic sea ice model forced with the data set developed in this study. *Huwald et al.*'s [2005] results provide further evidence for the internal consistency of the proposed data set.

[77] Internal snow and ice temperature observations from the Pittsburgh mass balance site are also used to derive a

snow thickness exploiting the fact that there is a change in temperature gradient at the snow-air interface. The snow depth reconstructed from this method (mean: 32 cm) is consistent with the snow depth inferred from matching the observed skin temperature with the thermistor temperatures in the snow. However, it is much larger than the snow depth computed using precipitation data (mean: 14 cm, assuming a reference snow density of 330 kg m^{-3}), or the mean of the three gauge measurements made only a few meters away from the thermistor string location (mean: 21 cm). Since measurements of snow depth at SHEBA show high variability at small spatial scales, snow depth from the nearby gauges is not necessarily representative of the snow thickness at that location. Instead, snow depth derived from internal temperature profiles are considered more reliable.

[78] Heat conduction in the snow is a combined process of pure conduction and heat transfer by nonconductive processes such as advective heat transport, and latent heat transport associated with water vapor diffusion. Considering such processes result in an "effective" heat conduction which can be noticeably larger than the pure thermal conduction alone. Measured internal snow and ice temperature profiles are used to calculate temperature gradients and conductive heat fluxes at the snow-ice interface. Assuming continuity of the conductive heat fluxes at the snow-ice interface, effective snow thermal conductivities are derived at four different SHEBA mass balance sites (Baltimore, Pittsburgh, Quebec 1 and Seattle).

[79] The conductivities derived using this method range from 0.40 to $0.50 \text{ Wm}^{-1} \text{ K}^{-1}$, with a mean of $0.47 \text{ Wm}^{-1} \text{ K}^{-1}$. At Pittsburgh, a value of $0.50 \text{ Wm}^{-1} \text{ K}^{-1}$ is derived. These values are larger than the value of $0.31 \text{ Wm}^{-1} \text{ K}^{-1}$ commonly used in global climate models, and the snow thermal conductivity of $0.14 \text{ Wm}^{-1} \text{ K}^{-1}$ derived from in situ measurements at SHEBA. The high spatial variability of the snow and ice thickness can result in horizontal temperature gradients. This is not considered in the simple 1-D heat conduction analysis presented here assuming the continuity of heat fluxes at the snow-ice interface. However, results from a 2-D heat conduction model show that the errors due to 2-D effects in the derived snow thermal conductivities are about 10–15%.

[80] To evaluate the internal consistency of the new proposed data set, a complete surface and basal energy budget is calculated. These budgets can be considered another means of estimating residual errors in the proposed forcing and validation data set. The surface energy budget shows a mean energy deficit of 3.5 Wm^{-2} during winter (October–March), and a mean surplus of 6.4 Wm^{-2} during summer (April–September). The total annual imbalance amounts to 1.6 Wm^{-2} . The winter difference is a consequence of an imbalance of the net atmospheric flux and the conductive heat flux at the surface. Errors in the conductive heat flux are mainly associated with the low vertical resolution of thermistor temperature profiles and snow/ice thickness measurements. The summer difference results from an imbalance between the net atmospheric flux and the energy of melt which is determined from observed melt rates. Considering the corrected snow thickness definition, snow thermal conductivity and ice base evolution, the

budget is considered self-consistent assuming errors in measurements.

[81] The ocean heat flux in the basal energy budget is calculated as a residual of the conductive heat flux into the ice and the energy of melt at the ice base. In winter, the ocean heat flux is generally low except during large wind events when ocean mixing is more vigorous. In summer, the ocean heat flux has its peak when shortwave radiation warms the surface waters through leads and through the ice. The ocean heat fluxes calculated at 6 different SHEBA mass balance sites are remarkably consistent, and agree reasonably well with ocean heat fluxes derived from turbulence measurements and from a bulk formulation. The ocean heat flux calculated with the residual method depends on the assumed salinity of newly formed ice, through the temperature and salinity dependence of the thermal conductivity and latent heat of fusion. Therefore these assumptions should be stated when providing ocean heat fluxes derived from the residual of other heat flux components for model validation purposes.

[82] **Acknowledgments.** The authors thank the SHEBA principal investigators of the Atmospheric Surface Flux Group (E. L. Andreas, C. W. Fairall, P. S. Guest, P. O. G. Persson), the Ice Physics Group (D. K. Perovich, B. C. Elder, J. Holmgren, J. A. Richter-Menge, M. Sturm, W. B. Tucker), and M. G. McPhee for providing the observational data. In addition we thank G. M. Flato for providing the SIMIP2 forcing data. We also thank two anonymous reviewers for their helpful suggestions to improve the manuscript. During this work, H.H. was supported by the Swiss National Science Foundation, grant 21-59243.99. L.-B.T. was supported by National Science Foundation grants OPP 98-18711 and OPP 02-30264. This is Lamont-Doherty Earth Observatory contribution 6698.

References

- Andreas, E. L., P. S. Guest, P. O. G. Persson, C. W. Fairall, T. W. Horst, R. E. Moritz, and S. R. Semmer (2002), Near-surface water vapor over polar sea ice is always near ice saturation, *J. Geophys. Res.*, *107*(C10), 8033, doi:10.1029/2000JC000411.
- Bitz, C. M., and W. H. Lipscomb (1999), An energy-conserving thermodynamic model of sea ice, *J. Geophys. Res.*, *104*, 15,669–15,677.
- Claffey, K. A., E. L. Andreas, D. K. Perovich, C. W. Fairall, P. S. Guest, and P. O. G. Persson (1999), Surface temperature measurements at SHEBA, paper presented at the Fifth Conference on Polar Meteorology and Oceanography, Am. Meteorol. Soc., Dallas, Tex.
- Colbeck, S. C. (1997), Model of wind pumping for layered snow, *J. Glaciol.*, *43*, 60–65.
- Colony, R., V. Radionov, and F. J. Tanis (1998), Measurements of precipitation and snow pack at Russian North Pole drifting stations, *Polar Record*, *34*, 3–14.
- Comiso, J. C., P. Wadhams, W. B. Krabill, R. N. Swift, J. P. Crawford, and W. B. Tucker III (1991), Top/bottom multisensor remote sensing of Arctic Sea ice, *J. Geophys. Res.*, *96*, 2693–2709.
- Cox, G. F. N., and W. F. Weeks (1988), Numerical simulations of the profile properties of undeformed first-year sea ice during the growth season, *J. Geophys. Res.*, *93*, 12,449–12,460.
- Déry, S. J., and L. B. Tremblay (2004), Modeling the effect of wind redistribution on the snow mass budget of polar sea ice, *J. Phys. Oceanogr.*, *34*, 258–271.
- Déry, S. J., and M. K. Yau (2002), Large-scale mass balance effects of blowing snow and surface sublimation, *J. Geophys. Res.*, *107*(D23), 4679, doi:10.1029/2001JD001251.
- Ebert, E. E., and J. A. Curry (1993), An intermediate one-dimensional thermodynamic sea ice model for investigating ice-atmosphere interactions, *J. Geophys. Res.*, *98*, 10,085–10,109.
- Eicken, H., H. R. Krouse, D. Kadko, and D. K. Perovich (2002), Tracer studies of pathways and rates of meltwater transport through Arctic summer sea ice, *J. Geophys. Res.*, *107*(C10), 8046, doi:10.1029/2000JC000583.
- Flato, G. M., and R. D. Brown (1996), Variability and climate sensitivity of landfast Arctic sea ice, *J. Geophys. Res.*, *101*, 25,767–25,777.
- Huwald, H., L.-B. Tremblay, and H. Blatter (2005), A multilayer sigma-coordinate thermodynamic sea ice model: Validation against Surface Heat Budget of the Arctic Ocean (SHEBA)/Sea Ice Model Intercomparison Project Part 2 (SIMIP2) data, *J. Geophys. Res.*, C05010, doi:10.1029/2004JC002328.
- Jordan, R. E., E. A. Andreas, C. W. Fairall, A. A. Grachev, P. S. Guest, J. M. Hanesiak, D. K. Perovich, and P. O. G. Persson (2003), Modeling surface exchange and heat transfer for the shallow snow cover at SHEBA, paper presented at the Seventh Conference on Polar Meteorology and Oceanography, Am. Meteorol. Soc., Hyannis, Mass.
- Makshtas, A. P., E. L. Andreas, P. N. Svyashchennikov, and V. F. Timachev (1999), Accounting for clouds in sea ice models, *Atmos. Res.*, *52*, 77–113.
- Maykut, G. A., and M. G. McPhee (1995), Solar heating of the Arctic mixed layer, *J. Geophys. Res.*, *100*, 24,691–24,703.
- Maykut, G. A., and N. Untersteiner (1971), Some results from a time dependent thermodynamic model of sea ice, *J. Geophys. Res.*, *76*, 1550–1575.
- McPhee, M. G. (2002), Turbulent stress at the ice/ocean interface and bottom surface hydraulic roughness during the SHEBA drift, *J. Geophys. Res.*, *107*(C10), 8037, doi:10.1029/2000JC000633.
- McPhee, M. G., and T. P. Stanton (1996), Turbulence in the statically unstable oceanic boundary layer under Arctic leads, *J. Geophys. Res.*, *101*, 6409–6428.
- McPhee, M. G., and N. Untersteiner (1982), Using sea ice to measure vertical flux in the ocean, *J. Geophys. Res.*, *87*, 2071–2074.
- McPhee, M. G., T. P. Stanton, J. H. Morison, and D. G. Martinson (1998), Freshening of the upper ocean in the Arctic: Is perennial sea ice disappearing?, *Geophys. Res. Lett.*, *25*, 1729–1732.
- McPhee, M. G., T. Kikuchi, J. H. Morison, and T. P. Stanton (2003), Ocean-to-ice heat flux at the North Pole environmental observatory, *Geophys. Res. Lett.*, *30*(24), 2274, doi:10.1029/2003GL018580.
- Notz, D., M. G. McPhee, M. G. Worster, G. A. Maykut, K. H. Schlünzen, and H. Eicken (2003), Impact of underwater-ice evolution on Arctic summer sea ice, *J. Geophys. Res.*, *108*(C7), 3223, doi:10.1029/2001JC001173.
- Ohmura, A. (1984), Comparative energy balance study for Arctic tundra, sea surface glaciers and boreal forests, *Geo J.*, *8*, 221–228.
- Perovich, D. K., and B. C. Elder (2001), Temporal evolution of Arctic sea-ice temperature, *Ann. Glaciol.*, *33*, 207–211.
- Perovich, D. K., and B. C. Elder (2002), Estimates of the ocean heat flux at SHEBA, *Geophys. Res. Lett.*, *29*(9), 1344, doi:10.1029/2001GL014171.
- Perovich, D. K., W. B. Tucker III, and R. A. Kurshfield (1989), Oceanic heat flux in the Fram Strait measured by a drifting buoy, *Geophys. Res. Lett.*, *16*, 995–998.
- Perovich, D. K., B. C. Elder, and J. A. Richter-Menge (1997), Observations of the annual cycle of sea ice temperature and mass balance, *Geophys. Res. Lett.*, *24*, 555–558.
- Perovich, D. K., et al. (1999a), Year on ice gives climate insights, *Eos Trans. AGU*, *80*(41), 481, 485–486.
- Perovich, D. K., T. C. Grenfell, B. Light, J. A. Richter-Menge, M. Sturm, W. B. Tucker III, H. Eicken, G. A. Maykut, and B. Elder (1999b), *SHEBA: Snow and Ice Studies* [CD-ROM], Cold Regions Res. and Eng. Lab., Hanover, N. H.
- Perovich, D. K., J. A. Richter-Menge, and W. B. Tucker III (2001), Seasonal changes in Arctic sea-ice morphology, *Ann. Glaciol.*, *33*, 171–176.
- Perovich, D. K., T. C. Grenfell, B. Light, and P. V. Hobbs (2002a), Seasonal evolution of the albedo of multiyear Arctic sea ice, *J. Geophys. Res.*, *107*(C10), 8044, doi:10.1029/2000JC000438.
- Perovich, D. K., W. B. Tucker III, and K. A. Ligett (2002b), Aerial observations of the evolution of ice surface conditions during summer, *J. Geophys. Res.*, *107*(C10), 8048, doi:10.1029/2000JC000449.
- Perovich, D. K., T. C. Grenfell, J. A. Richter-Menge, B. Light, W. B. Tucker III, and H. Eicken (2003), Thin and thinner: Sea ice mass balance measurements during SHEBA, *J. Geophys. Res.*, *108*(C3), 8050, doi:10.1029/2001JC001079.
- Persson, P. O. G., C. W. Fairall, E. L. Andreas, P. S. Guest, and D. K. Perovich (2002), Measurements near the Atmospheric Surface Flux Group tower at SHEBA: Near-surface conditions and surface energy budget, *J. Geophys. Res.*, *107*(C10), 8045, doi:10.1029/2000JC000705.
- Schramm, J. L., G. M. Flato, and J. A. Curry (2000), Toward the modeling of enhanced basal melting in ridge keels, *J. Geophys. Res.*, *105*, 14,081–14,092.
- Sturm, M., J. Holmgren, M. König, and K. Morris (1997), The thermal conductivity of seasonal snow, *J. Glaciol.*, *143*, 26–41.
- Sturm, M., J. Holmgren, and D. K. Perovich (2001), Spatial variations in the winter heat flux at SHEBA: Estimates from snow-ice interface temperatures, *Ann. Glaciol.*, *33*, 213–220.

- Sturm, M., J. Holmgren, and D. K. Perovich (2002a), Winter snow cover on the sea ice of the Arctic Ocean at the Surface Heat Budget of the Arctic Ocean (SHEBA): Temporal evolution and spatial variability, *J. Geophys. Res.*, *107*(C10), 8047, doi:10.1029/2000JC000400.
- Sturm, M., D. K. Perovich, and J. Holmgren (2002b), Thermal conductivity and heat transfer through the snow on the ice of the Beaufort Sea, *J. Geophys. Res.*, *107*(C10), 8043, doi:10.1029/2000JC000409.
- Uttal, T., et al. (2002), Surface Heat Budget of the Arctic Ocean, *Bull. Am. Meteorol. Soc.*, *83*, 255–275.
- Walsh, J. E., and W. L. Chapman (1998), Arctic cloud-radiation-temperature associations in observational data and atmospheric reanalyses, *J. Clim.*, *11*, 3030–3045.
- Walsh, J. E., V. K. D. Portis, and V. Meleshko (1998), Arctic precipitation and evaporation: Model results and observational estimates, *J. Clim.*, *11*, 72–87.
- Wettlaufer, J. S. (1991), Heat flux at the ice-ocean interface, *J. Geophys. Res.*, *96*, 7215–7236.
- Wettlaufer, J. S., N. Untersteiner, and R. Colony (1990), Estimating oceanic heat flux from sea ice thickness and temperature data, *Ann. Glaciol.*, *14*, 315–318.
- Yang, D. (1999), An improved precipitation climatology for the Arctic Ocean, *Geophys. Res. Lett.*, *26*, 1625–1628.
-
- H. Blatter, Institute for Atmospheric and Climate Science, Swiss Federal Institute of Technology, Winterthurerstrasse 190, CH-8057 Zurich, Switzerland. (blatter@env.ethz.ch)
- H. Huwald, Environmental Fluid Mechanics Laboratory, Ecole Polytechnique Fédérale de Lausanne, Station 2, CH-1015 Lausanne, Switzerland. (hendrik.huwald@epfl.ch)
- L.-B. Tremblay, Lamont-Doherty Earth Observatory of Columbia University, Route 9W, Palisades, NY 10964-8000, USA. (tremblay@ldeo.columbia.edu)